

# Morphological Classification of Radio Galaxies with wGAN-supported Augmentation

Lennart Rustige<sup>1,2,\*</sup>, Janis Kummer<sup>1,3,†</sup>, Florian Giese<sup>1,4,5,‡</sup>, Kerstin Borrás<sup>2,6</sup>, Marcus Brüggén<sup>3</sup>, Patrick L. S. Connor<sup>1,7</sup>, Frank Gaede<sup>2</sup>, Gregor Kasieczka<sup>7</sup>, Tobias Knopp<sup>4,5</sup> and Peter Schleper<sup>7</sup>

<sup>1</sup> Center for Data and Computing in Natural Sciences (CDCS), Notkestrasse 9, D-22607 Hamburg, Germany

<sup>2</sup> Deutsches Elektronen-Synchrotron DESY, Notkestrasse 85, D-22607 Hamburg, Germany

<sup>3</sup> Universität Hamburg, Hamburger Sternwarte, Gojenbergsweg 112, D-21029 Hamburg, Germany

<sup>4</sup> Section for Biomedical Imaging, University Medical Center Hamburg-Eppendorf, D-20246 Hamburg, Germany

<sup>5</sup> Institute for Biomedical Imaging, Hamburg University of Technology, D-21073 Hamburg, Germany

<sup>6</sup> RWTH Aachen University, Templergraben 55, D-52062 Aachen, Germany

<sup>7</sup> Universität Hamburg, Institut für Experimentalphysik, Luruper Chaussee 149, D-22761 Hamburg, Germany

Accepted XXX. Received YYY; in original form ZZZ

## ABSTRACT

Machine learning techniques that perform morphological classification of astronomical sources often suffer from a scarcity of labelled training data. Here, we focus on the case of supervised deep learning models for the morphological classification of radio galaxies, which is particularly topical for the forthcoming large radio surveys. We demonstrate the use of generative models, specifically Wasserstein Generative Adversarial Networks (wGANs), to generate data for different classes of radio galaxies. Further, we study the impact of augmenting the training data with images from our wGAN on three different classification architectures. We find that this technique makes it possible to improve models for the morphological classification of radio galaxies. A simple Fully Connected Neural Network (FCN) benefits most from including generated images into the training set, with a considerable improvement of its classification accuracy. In addition, we find it is more difficult to improve complex classifiers. The classification performance of a Convolutional Neural Network (CNN) can be improved slightly. However, this is not the case for a Vision Transformer (ViT).

**Key words:** radio continuum: galaxies – methods: statistical – techniques: image processing – methods: data analysis

## 1 INTRODUCTION

Radio galaxies are galaxies that emit a large fraction of their electromagnetic output in the radio band. The structures visible in radio wavelengths are typically larger than the structures visible in optical wavelengths. Radio galaxies are a class of active galactic nuclei (AGN) and are powered by supermassive black holes at the centres of galaxies. The extended emission is produced by synchrotron radiation of highly relativistic particles accelerated by the AGN. Studying radio galaxies helps to understand the effects of massive black holes on their environment (see e.g. McNamara & Nulsen (2007)). The jets of highly energetic particles emitted by giant radio galaxies potentially play a major role in the creation of cosmic magnetic fields (Vazza et al. 2022).

A lot of new radio sources will be discovered with the new generation of radio telescopes (e.g. LOFAR, MeerKAT, and in the future the SKA (van Haarlem & et al. 2013; Jonas & MeerKAT Team 2016; Carilli et al. 2004)). Processing the incoming data is one of the biggest challenges in radio astronomy. The cause is not only the enormous

amount of data, but also the higher source density due to the improved sensitivity of the instruments. Novel techniques are required for this purpose. Deep learning has proven to be useful for automation of data processing, but commonly requires large amounts of labelled training data for supervised algorithms, which are not always available. For instance, the SKA data challenges have demonstrated the difficulties of source finding for SKA data (Bonaldi & et al. 2021).

Morphological classification of radio sources can be achieved by deep learning models trained on well-understood data sets. Aniyán & Thorat (2017); Alhassan et al. (2018); Tang et al. (2019); Samudre et al. (2021); Maslej-Krešňáková et al. (2021) use Convolutional Neural Networks (CNNs) trained on data from the FIRST (Faint Images of the Radio Sky at Twenty-Centimeters) survey Becker et al. (1995) for the classification of radio galaxies. The architectures of the neural networks for classification are inspired by the Alexnet (Krizhevsky et al. 2012). For other approaches in radio galaxy classification, see e.g. Lukic et al. (2019); Bowles et al. (2020); Scaife & Porter (2021); Sadeghi et al. (2021); Ma et al. (2019); Wu et al. (2019).

In other areas of astronomy, similar morphological classification problems arise, e.g. for classification of optical galaxies (Lintott et al. 2008; Nair & Abraham 2010), and of gravitational lenses (Petrillo et al. 2017). Here supervised methods of machine learning have been

\* E-mail: lennart.rustige@desy.de

† E-mail: janis.kummer@uni-hamburg.de

‡ E-mail: florian.giese@tuhh.de

applied with some success, see e.g. [Cheng et al. \(2020\)](#); [Vavilova et al. \(2021\)](#).

However, the existing number of radio sources with morphological labels is limited ( $\approx 1300$  in the MiraBest data set with two classes ([Porter 2020](#))). These class labels are typically extracted from catalogues created and curated manually by experts. Small data sets used in the training of deep learning models for galaxy classification can be enlarged by data augmentation, e.g. by applying random rotations and reflections to the images (classical augmentation). A different approach based on equivariance implements the symmetry constraints of the problem directly in the construction of the model ([Bowles et al. 2021](#); [Scaife & Porter 2021](#)). This may help classifiers to understand symmetries without relying exclusively on augmentation and may be particularly useful for problems with sparse data.

In this work, we investigate a novel application of generative models to enhance the available training sets. For this augmentation technique, multiple neural networks are combined to learn the underlying distribution of a data set. We focus on the task of classifying different morphological types of radio galaxies. The morphological classification scheme by Fanaroff-Riley is fundamental for such applications ([Fanaroff & Riley 1974](#)). For the class FRI, the unique maximum of the radio emission resides in the centre of the source and the surface brightness decreases along the jets. For FR II sources, the two maxima of the radio emissions are located at the edges of the jets and the surface brightness in the centre is lower. As radio sources have a large variety of structures, we consider two more classes. Unresolved and point sources are contained in the Compact class. The Bent class consists of sources for which the angle between the jets differs significantly from 180 degrees. The two sub-types narrow-angle tail (NAT) and wide-angle tail (WAT) are further discriminated by the angle, but are fully subsumed in the Bent class for this study. As in [Alhassan et al. \(2018\)](#); [Samudre et al. \(2021\)](#), we study a four-class classification problem, including bent-tail and compact sources in addition to the classes FRI and FR II of [Fanaroff & Riley \(1974\)](#). [Figure 1](#) illustrates the considered classes (FRI, FR II, Compact, and Bent).

In this study, we investigate whether different radio galaxy classifiers can be improved when training is supported by providing additional data generated with a Wasserstein Generative Adversarial Network (wGAN). For similar approaches from different fields see, for example, [Frid-Adar et al. \(2018\)](#); [Zhu et al. \(2017\)](#); [Gowal et al. \(2021\)](#). We extend our framework presented in [Kummer et al. \(2022\)](#) to handle larger ratios between real and generated images. Additional images are only generated when they are needed during training. As before, we start with a simple model, namely a Fully Connected Neural Network (FCN). In addition, we apply wGAN-supported augmentation to a CNN and a Vision Transformer (ViT) ([Dosovitskiy et al. 2020](#)).

The long-term goal is to use classification models to process incoming data from new radio telescopes. For this purpose, classification models need to generalise particularly well. A common problem in astronomy is the scarcity of labelled data in the face of large amounts of new data to process. This is a very different situation as for instance in particle physics, where simulations are highly fine-tuned and experiments are constantly repeated. In particular, for forthcoming radio surveys, and even for the majority of sources in FIRST, no morphological labels are available. As a result unsupervised, semi-supervised and self-supervised methods have gained attention without reaching the performance of supervised methods ([Mostert et al. 2021](#); [Slijepcevic et al. 2022](#); [Slijepcevic et al. 2022](#)). The current classification scheme of radio galaxies and our physical

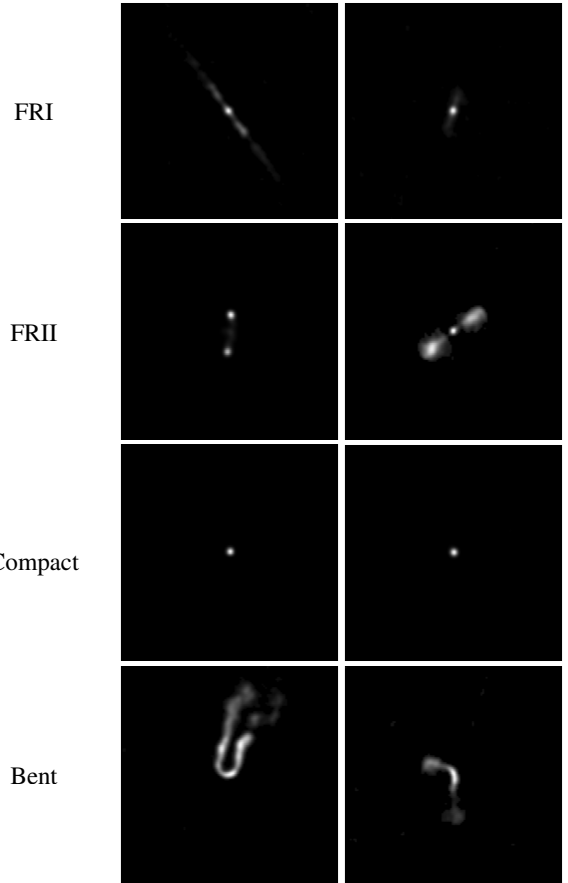


**Figure 1.** Class definition for FRI, FR II, Compact and Bent. For the Bent class we show an example of a NAT source in the left and a WAT source in the right panel.

**Table 1.** Number of radio galaxy images per class in the train, validation and test data sets.

	FRI	FR II	Compact	Bent	Total
5-fold cross train	316	659	232	198	1405
5-fold cross valid	79	165	59	50	353
test	100	100	100	100	400
total	495	924	391	348	2158
relative frequency in total	0.23	0.43	0.18	0.16	1

interpretation will be challenged by new radio surveys (see e.g. [Mingo et al. \(2019\)](#)). Discoveries of rare morphologies can help to extend our understanding of radio sources, but are potentially prohibited by supervised learning techniques.

This paper is organised as follows: In [section 2](#), we introduce the data set used for training, validation, and testing. The generative model and its implementation are described in [section 3](#). The training procedure and the assessment of image quality are discussed in [section 4](#). The results of the comparison between only classical and classical plus wGAN-supported augmentation for different classifiers are presented in [section 5](#) before we conclude in [section 6](#).

## 2 DATA

We combined different catalogues [Gendre & Wall \(2008\)](#); [Gendre et al. \(2010\)](#); [Miraghaei & Best \(2017\)](#); [Capetti et al. \(2017b,a\)](#); [Baldi et al. \(2017\)](#); [Proctor \(2011\)](#) that characterise radio sources from the FRIST survey to create a data set of 2158 radio galaxy images with morphological labels. The labelling in the catalogues is typically performed by experts by considering radio images and the corresponding optical counterparts. We group radio sources in 4 classes, namely FRI, FRII, Compact and Bent. The data set is published on zenodo [Griese et al. \(2022\)](#) and on GitHub (<https://github.com/floriangriese/RadioGalaxyDataset>). The radio galaxy images of the FIRST survey are collected from the virtual observatory skyview<sup>1</sup>. We downloaded the original images with a size of 300 x 300 pixels. Then we adopted the preprocessing from [Aniyan & Thorat \(2017\)](#) after cropping the images to the input size of our generative network (128 x 128 pixels). In particular, we set all pixel values below three times the local RMS noise to the value of this threshold. Subsequently, the pixel values were rescaled to the range between -1 and 1 to represent floating point greyscale images. Finally, we applied classical augmentation to each image of the training set during training.

We separated 100 sources per class from the data set for the final evaluation of our models. For validation purposes during training (e.g. choosing the best model), we use a 5-fold cross-validation. Therefore, we do not need a separate validation set. As a result, we lose less training data. In particular, we split the training set into five blocks and did five separate training runs. For each of these runs one of the five blocks was used as the validation set and the remaining four blocks represented the corresponding training set. The quantities per class and per split are shown in [Table 1](#).

## 3 WASSERSTEIN GAN

The ability to learn representations of underlying statistical distributions of data sets makes generative models a powerful tool for the creation of additional data points. In particular, sampling from those representations allows to speed up conventional simulation techniques significantly and may be useful for further subsequent treatments ([Buhmann et al. 2021, 2022](#)).

Three different categories of generative models are well-established: generative adversarial networks (GANs), variational autoencoders (VAEs), and flow-based models. Diffusion models represent a relatively new development in this area. In this work, we focus on GANs. They consist of two neural networks: a generator  $G$  that generates fake images from a noise vector  $Z$  and the discriminator  $D$  that discriminates between real and fake images. This architecture was first introduced in [Goodfellow et al. \(2014\)](#); [Salimans et al. \(2016\)](#). In a two-player minimax game, the generator learns to create fake images, which become less and less distinguishable from the real ones in the course of the training. The loss function for this setup reads ([Goodfellow et al. 2014](#); [Salimans et al. 2016](#)):

$$L = \min_G \max_D \mathbb{E}[\log D(x)] + \mathbb{E}[\log(1 - D(G(z)))], \quad (1)$$

where  $x$  represent real samples and  $G(z) = \tilde{x}$  generated samples.

For this project, we employ a variant of the standard GAN setup called wGAN that uses the Wasserstein-1 metric, also referred to

as the Earth Mover's distance, as main term in the loss function ([Arjovsky et al. 2017](#)). This loss function is calculated as

$$L = \sup_{f \in \text{Lip}_1} \{\mathbb{E}[f(x)] - \mathbb{E}[f(\tilde{x})]\}, \quad (2)$$

where  $f$  denotes a 1-Lipschitz function that is learned during the training procedure. The discriminator of a standard GAN is transformed into a critic and is used to estimate the Wasserstein distance between real and generated images. Hence, the absolute value of the loss function is correlated with the image quality, resulting in the name change. Additionally, the training of wGANs is often more stable and more likely to converge than standard GAN setups. To approximate the Wasserstein-1 metric by use of a critic network, it has to be ensured that the 1-Lipschitz constraint is fulfilled. This is achieved by applying a gradient penalty term to the loss function as in [Gulrajani et al. \(2017\)](#)

$$L = \lambda \mathbb{E}[(\|\nabla_{\tilde{x}} f(\tilde{x})\|_2 - 1)^2] \quad (3)$$

for random samples  $\tilde{x} \sim \mathbb{P}_{\tilde{x}}$ .

Since we work with image data, it has proven to be the most promising approach to construct a wGAN setup based on convolutional layers ([Radford et al. 2015](#)). The generator receives a noise tensor of size 100x1 and a class label  $y$  and, through multiple layers of 2D transposed convolution operators, enlarges this to a 128x128 tensor, consistent with the dimensions of real images. The critic is given either real or generated images, as well as the class label  $y$ . The output of the critic is a single real value, which represents the belief of the critic for the image to be real. Generator and critic are trained intermittently, where the critic has five training cycles per training cycle of the generator. While training the generative model, it is necessary to apply classical augmentation such that the symmetries of the training set are also present in the generated data sets, and to avoid introducing a bias due to the limited number of training examples.

Morphologies of radio galaxies are diverse and result in very different images. Consequently, it is reasonable to condition the networks with the class label  $y$  such that a combination of image and class label is provided to the networks. In particular, this allows applying supervised learning techniques on the output of the generator. For our setup, this is achieved for the generator by applying a 2D transposed convolution operator on a matrix of image dimensions filled with the class label. The transpose-convoluted layer is then concatenated to the first transpose-convoluted layer of the noise tensor. Batch normalisation in 2D and ReLU activation functions are used. The concatenated tensor is then passed through five additional 2D transposed convolutions, where no normalisation or activation is applied after the last layer. Instead, the individual pixel values are clipped to  $[-1, 1]$  for conversion to grayscale. The critic is built analogously, but uses 2D convolutional layers, resulting in a single output node representing the critic score for image quality. Here, layer normalisation and leaky ReLU functions are used except for the last layer. A schematic of the wGAN setup can be found in [Figure 2](#).

## 4 RESULTS OF IMAGE GENERATION WITH A WGAN

### 4.1 Training

For each choice of training and validation data in the cross-validation procedure a wGAN training run is launched on the corresponding training set. The training is performed with a single NVIDIA A100 GPU provided by the Maxwell cluster at DESY for 40k generator

<sup>1</sup> <https://skyview.gsfc.nasa.gov>

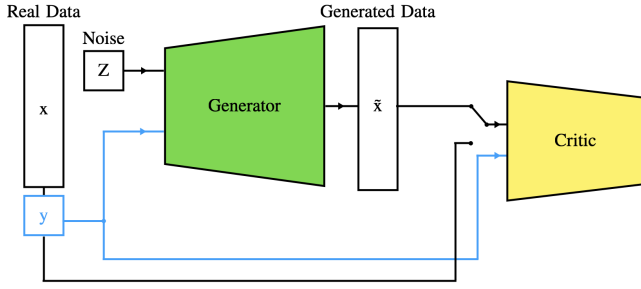


**Figure 2.** Schematic of the wGAN architecture, where  $y$  denotes the class label of real  $x$  or generated images  $\tilde{x}$

iterations. A batch size of 400 is chosen and one training run takes roughly seven hours to complete. The generator and critic weights are saved every 250 iterations, allowing to scan for the best training state later on, as described in the following section.

## 4.2 Evaluation of image quality

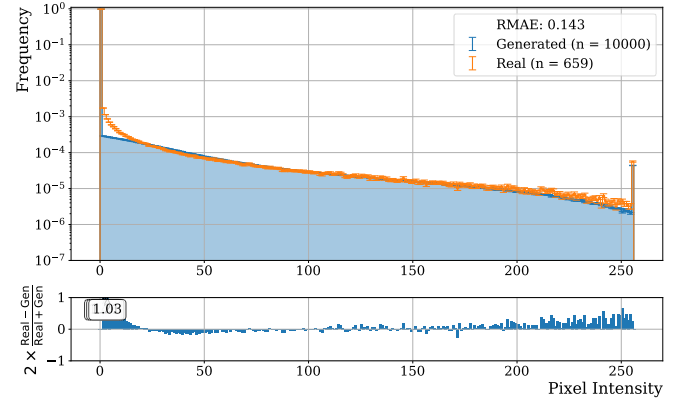
In this section, we present images created using the generator of the wGAN and examine the quality of the generated images in several ways.

### 4.2.1 Distribution-based comparison

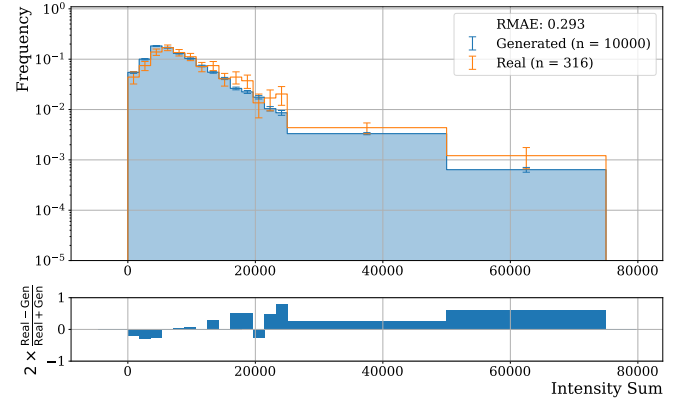
We define a set of distributions to compare generated images with the training data set, in order to determine the quality of generated images and thus to find the best performing training iteration. This includes normalised histograms of pixel intensities, the number of pixels with an intensity greater than zero and of the sum of intensities. These histograms are compared for each class individually and the relative mean absolute error (RMAE) between the generated set of 10k images and the training set is computed. The RMAEs for the different distributions are summed up to yield a single figure-of-merit (FOM), where the wGAN training iteration with the lowest FOM value is used in the following. This procedure is followed for each of the four classes separately, i.e. we allow a different iteration of the generator training to yield the best model for each class.

Arbitrarily chosen examples of these distributions are shown in Figure 3, where the distribution of the real images is shown in orange and the distribution of the generated images in blue. The uncertainty for each bin is given by the square-root of entries in that bin before normalisation. The bottom panels in this figure show the per-bin divergence between the distributions, where absolute deviations larger than 1 are indicated by the corresponding value written in boxes. Here, only examples from the first cross-validation fold (of five) are shown.

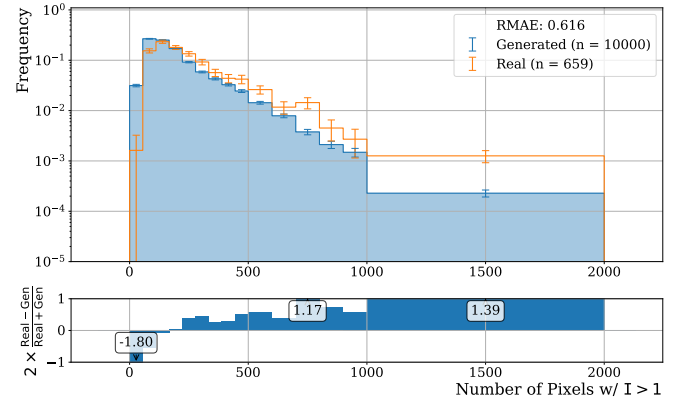
Overall, the distributions of the generated images tend to follow the distribution of the real images. Nevertheless, the generated images have difficulties in recreating very low, but non-zero, intensities. This can be seen for pixel values between 1 and 20 in Figure 3a, which directly translates into under-representing the number of pixels with an intensity  $I > 0$  in Figure 3c.



(a) Pixel intensities of FRII sources.



(b) Sum of pixel intensities of FRI sources.



(c) Number of activated pixels of FRII sources.

**Figure 3.** Examples of image quality measures comparing histograms of real (orange) and generated (blue) images for the generator training epoch with the lowest combined RMAE for the corresponding class. The per-bin relative error is shown in the bottom of each panel. Histograms shown here are chosen arbitrarily from the first cross-validation fold.

### 4.2.2 Visual comparison

In order to get a visual idea of image quality, we generated a set of 5k images per class and compared them to the full training data set over all cross-validation folds. The images are rotated so that their principal components are aligned. Subsequently, we compute the pixel-by-pixel difference for all possible pairs of real and generated images. All classes also include a few difficult to define sources with

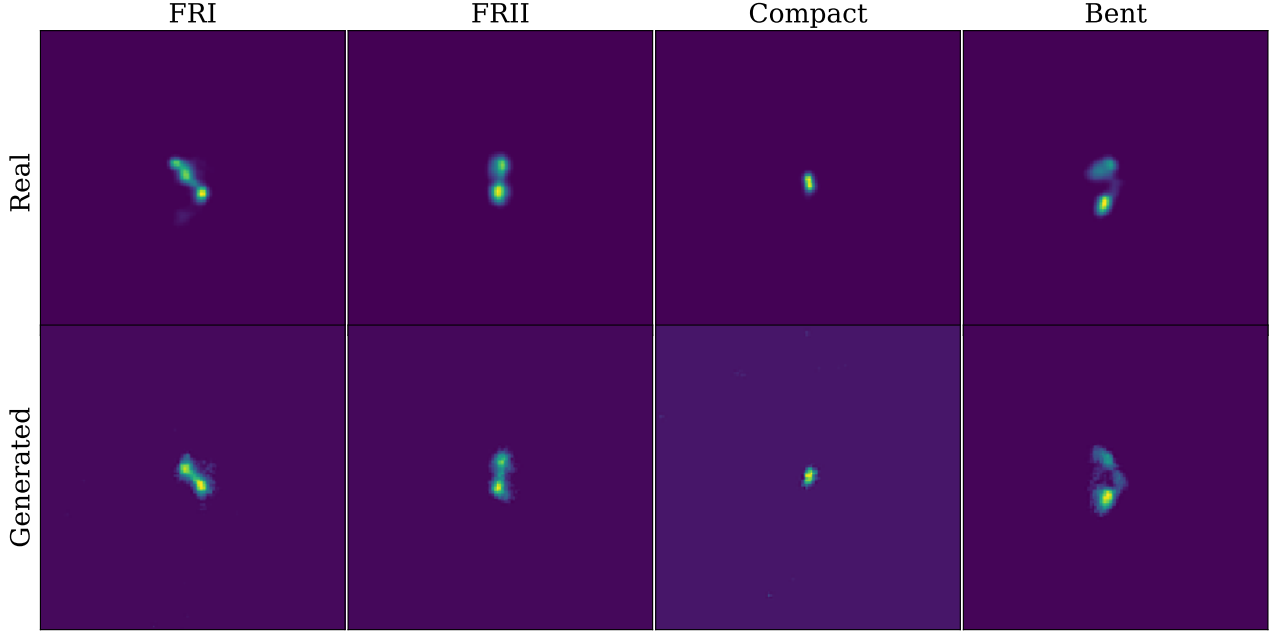


**Figure 4.** Closest matching pairs in terms of a pixelwise difference between generated and real images for each class. The set of real images is the full training data set over all cross-validation folds; the generated data set consists of 5k images per class. Images are aligned according to the first principal component.

rather small spatial extension that are easy to emulate but do not show the generator’s capability of reproducing the more interesting extended sources. Thus, we only consider images with an intensity sum of at least 15k (5k) for the extended (compact) radio galaxies. We show the resulting closest pairs for each class in Figure 4. By eye, the generated images appear very similar to the analogue real images, indicating a good performance of the generator setup. To also get an impression of the diversity of the generated data we show a random set of generated images in App. A.

#### 4.2.3 Classifier-based comparison

Next, we use a CNN trained solely on the data set of real images to assess the image quality further. We compare the performance of this classifier on the real test set and a set of generated images. The architecture of the CNN used for this experiment is summarised in Table B2. A comparison of the confusion matrices on both sets tests for any bias introduced by the image generation. In particular, we evaluate the conditioning on the class labels. First, we show in the top panel of Figure 5 the confusion matrix of the classifier on the real test. We compare this to the confusion matrix of the same classifier evaluated on the set of generated images on the bottom panel of Figure 5. We find that the class conditioning of the generated images works well overall. However, confusion for images of the class FRI with the predicted classes FRII is enhanced on the generated test set. The classification performance of the class Compact is deteriorated on the generated test set and particularly the confusion for images of the class Compact with the predicted class FRII is enhanced. As some FRII-like sources resemble a combination of two compact sources this is not surprising. Confusion for images of the class Bent with the predicted classes FRI is for instance slightly reduced.

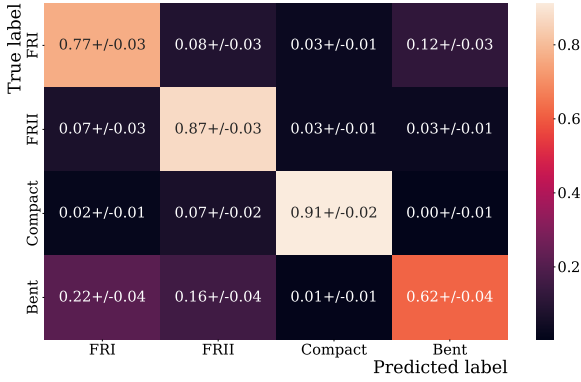
## 5 RESULTS OF CLASSIFIER TRAINING USING WGAN-SUPPORTED AUGMENTATION

We assess the new approach of supplementing the training set with generated images by comparing the performance of different classifiers (each trained on different setups with increasing amount of generated data). Our benchmark is the performance of the classifier trained on the original training set. We test the performance of the classifier trained with the original training set plus simulated images by the generator of the wGAN against this benchmark. We start with a FCN (see Table B1). Subsequently, we increase the complexity of the classifier by training a CNN (see Table B2). Finally, we apply our framework to a state-of-the-art classifier, namely the ViT (Dosovitskiy et al. 2020). We use the ViT-B\_16 vision transformer configuration with pre-trained weights from the ImageNet21k data set<sup>2</sup> with a resetted head layer. The GAN generated images with pixel sizes 128x128 are zero-padded up to 224x224 pixels to fit the pre-trained model input size. As a loss function, a weighted cross-entropy loss is implemented. As an attention based model, the ViT splits the image into fixed-size patches processed by the transformer encoder. The ViT is able to output attention maps. These illustrate regions considered important by the classifier. Therefore, attention maps help to understand the internal processes of the model.

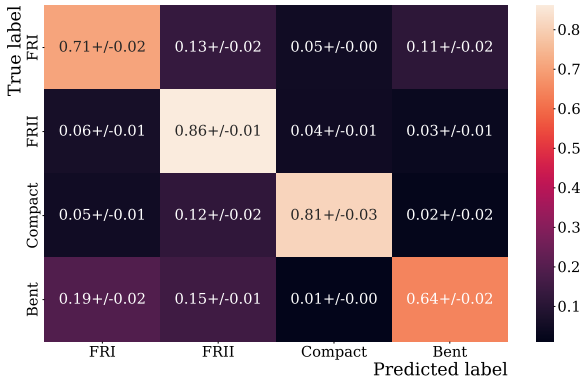
We generate images on the fly, i.e. each time a generated image is loaded it is newly generated. These setups are not optimised to reach maximal classification accuracies. The goal of this study is only to compare classical augmentation with wGAN-supported augmentation for each classifiers. We do not compare the performance of the three classifiers in detail either.

<sup>2</sup> For the adopted ViT implementation see <https://github.com/lucidrains/vit-pytorch> and for the corresponding weights see [https://github.com/google-research/vision\\_transformer](https://github.com/google-research/vision_transformer)





(a) Real test sample.



(b) Generated sample.

**Figure 5.** Confusion matrices on the real only test data set (above) and a data set of 4k generated images, where each of the generators pertaining to a cross-validation fold contributes 200 images per class (5 generators  $\times$  4 classes  $\times$  200 images). Matrices are row-wise normalised and both data sets are class balanced. The values represent the mean and standard deviation of the confusion matrices obtained from each of the classifiers trained on the cross-validation folds with classical augmentation only.

**Evaluation metrics** To compare the overall performance among different training setups and to determine the best training iteration of a classifier training run, we use the multi-class Brier score (Brier 1950). The Brier score is essentially the mean squared error of the predicted probabilities of a classifier for all classes. This has the advantage that also the certainty of the classifier’s decision is considered, which winner-takes-all FOMs such as accuracy do not take into account. For each setup, i.e. for a given ratio between the number of generated  $i_g$  and real images  $i_r$ , denoted  $\lambda = i_g/i_r$ , we have five models due to the 5-fold cross-validation.

The final evaluation is performed on an independent test set that contains real data only. We use the most commonly applied metric in radio astronomy publications: multi-class accuracy. In order to estimate statistical fluctuations, we average the performance metrics over the five best models of each cross-validation fold.

**Accuracy** The multi-class accuracy, i.e. number of correct classifications over number of all classifications, on the test data set is shown in Figure 7 for the three different classifiers investigated here. The results are shown for different training scenarios, where the number of generated images used to augment the training data set (represented by  $\lambda$ ) is varied. The blue markers (uncertainty bars) represent the mean (standard deviation) of the obtained results over

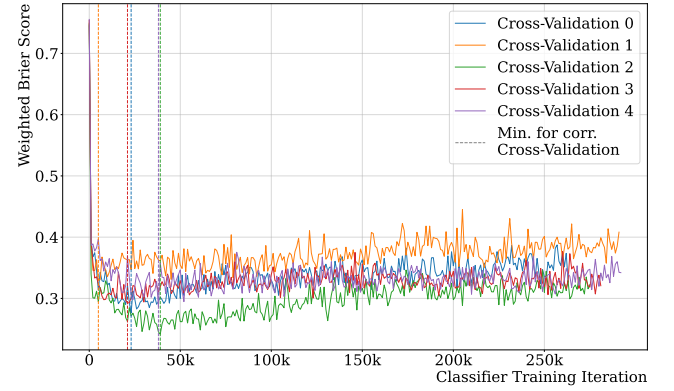


**Figure 6.** Weighted Brier score on the corresponding cross-validation validation sets per classifier training iteration. The iteration resulting in the minimum score is indicated by a dashed vertical line.

all cross-validation folds for the augmented training data sets and the horizontal orange line (area) show the corresponding result for the real data only case.

Figure 7a presents the results for the FCN, which yields an improvement in accuracy of  $(18 \pm 5) \%$  over the baseline setup at  $\lambda = 2$ . All augmented training setups outperform the real data only case which reaches an accuracy of  $(59 \pm 2) \%$ .

The highest obtained average for the CNN classifier is reached for  $\lambda = 3$ , as can be seen in Figure 7b, which is  $(3 \pm 2) \%$  higher than the real data only baseline at  $(79 \pm 1) \%$ . The highest obtained average using wGAN augmented training data for the ViT classifier is reached at  $\lambda = 2$ , see Figure 7c, which is  $(0.7 \pm 2.0) \%$  lower than the real data only baseline at  $(81 \pm 1) \%$ .

## 6 DISCUSSION AND CONCLUSION

Other studies probe the use of generative models to create images of radio galaxies (Ma et al. 2018, 2019; Bastien et al. 2021). These studies are based on Variational Autoencoders (VAEs), so that the approach used for the study presented here, utilising a wGAN, is, to our knowledge, novel to the field of radio astronomy.

We are able to generate highly realistic images of radio sources of the four different radio galaxy classes investigated for this study. For this, we rely on the good agreement between the image metric distributions, such as the pixel intensity histogram, between real and generated images, as well as the good agreement between the confusion of a CNN classifier trained only on real data obtained on a real data only test set and a generated data only test set. Particularly the latter, provides confidence for the class conditioning of the generator.

Following a visual inspection, we note that the generated images tend to have sharper edges, i.e. low intensity pixels directly next to high intensity pixels. This is not the case for real images, which are smeared due to detector resolution effects. Resolving these issues would yield even more realistic generated images.

However, we do not observe issues known from other state-of-the-art generative networks in radio astronomy, such as different noise levels between generated and training data or pseudo-textures and pseudo-structures. The results of this study therefore constitute a major improvement in generated image quality.

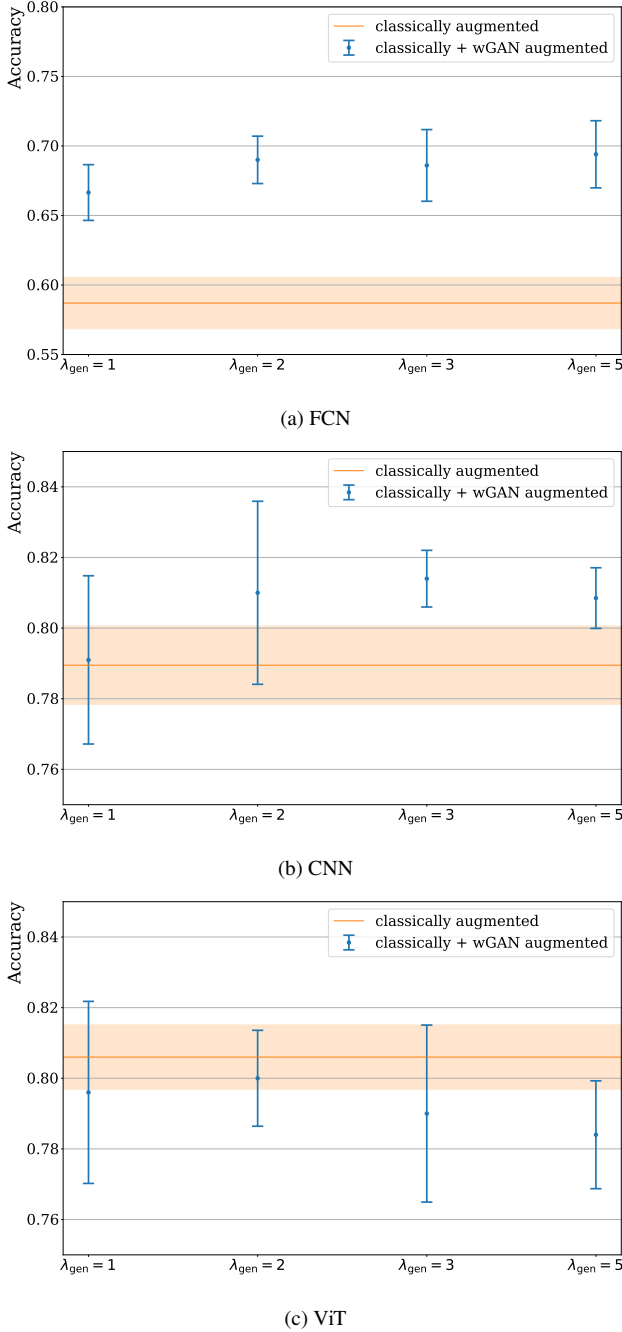


**Figure 7.** Accuracy on the test data set for the three different classifier architectures for different training scenarios, where the amount of generated images used to augment the training data set (represented by  $\lambda$ ) is varied. The blue markers (uncertainty bars) represent the mean (standard deviation) of the obtained results over all cross-validation folds for the classically + wGAN augmented training data sets and the horizontal orange line (area) show the corresponding result for the only classically augmented case.

This high quality of the images allows us to use them to improve the training of an external classifier, called wGAN-supported augmentation here. This represents an extension to realistic data of the studies done in [Butter et al. \(2021\)](#), which showed that statistical information contained in a simplistic toy training data set can be augmented using generative models. Another extension of this study to more realistic data in the field of particle physics is given in [Bieringer et al. \(2022\)](#).

Here, we are able to show that adding generated images to the training data set does clearly improve the classifier performance on a real data only test set for the FCN classifier, where the largest improvement of  $(18 \pm 5) \%$  over the baseline setup is reached for  $\lambda = 2$ , meaning a training data set consisting of all real images plus twice as many generated images. Additionally, similar improvements are seen for all other  $\lambda$  values that have been tested.

For the considerably more complex CNN classifier, the improvement is not so consistent and already the baseline performance is far better than even the enhanced performance of the FCN classifier. However, we do obtain a maximal improvement of  $(3 \pm 2) \%$  for  $\lambda = 3$ , which also represents the overall highest accuracy for any of the setups investigated here.

Finally, for the most complex classifier architecture, the ViT, we are not able to show a conclusive improvement of the classifier performance, so that we might expect a dependency of the ability of generated images to add useful information to the training data set on the baseline performance (often connected to the complexity) of the classifier in question. A naïve interpretation could be that the better performing architectures are simply more sensitive to even small differences between the real and generated images.

Further, we considered a three-class classification problem with extended sources only. We found that the overall accuracy is reduced as compact sources are easier to classify. More importantly, the significance of the improvement by including generated images in the training is not enhanced as the variations in the cross-validation tend to increase as well.

The best overall accuracy is obtained by using the CNN and wGAN augmented training data, but only by a small margin. Yet, we have shown that wGAN augmentation works in principle (similar to the goal in [Butter et al. \(2021\)](#), as noted above) and can significantly improve a somewhat simpler algorithm. This can be useful for applications of classification algorithms in resource-constrained environments, i.e. disk-space and inference time restrictions.

Given that our generative model is able to generate very quickly large sets of radio galaxy images of different morphologies, wGANs can play an important role in the simulation and analysis of large radio surveys. Future work involving much larger training sets from the LO-FAR telescope will explore this further. Moreover, wGAN-generated images can be used to validate new interferometric machine-learning algorithms, see e.g. [Schmidt et al. \(2022\)](#). To this end, we provide the model and weights with documentation at <https://github.com/floriangriese/wGAN-supported-augmentation>.

## ACKNOWLEDGEMENTS

This work was supported by UHH, DESY, TUHH and HamburgX grant LFF-HHX-03 to the Center for Data and Computing in Natural Sciences (CDCS) from the Hamburg Ministry of Science, Research, Equalities and Districts. This project benefits greatly from the exchange with particle physicists with a vast experience in using generative models for calorimeter simulations and was supported in part through the Maxwell computational resources operated at DESY.

## DATA AVAILABILITY

The code of all models trained for this work is publicly available on GitHub at the following address: <https://github.com/florian>

**griese/wGAN-supported-augmentation**

The data set is available on Zenodo at <https://doi.org/10.5281/zenodo.7120632> and code for data loading on GitHub at <https://github.com/floriangriese/RadioGalaxyDataset>. If you use this data set, please cite Griese et al. (2022).

**REFERENCES**

- Alhassan, W., Taylor, A. R., & Vaccari, M., 2018. The first classifier: compact and extended radio galaxy classification using deep convolutional neural networks, *MNRAS*, **480**(2), 2085–2093.
- Aniyan, A. K. & Thorat, K., 2017. Classifying radio galaxies with the convolutional neural network, *The Astrophysical Journal Supplement Series*, **230**(2), 20.
- Arjovsky, M., Chintala, S., & Bottou, L., 2017. Wasserstein gan.
- Baldi, R. D., Capetti, A., & Massaro, F., 2017. Fr0cat: a first catalog of fr 0 radio galaxies, *A&A*, **609**, A1.
- Bastien, D. J., Scaife, A. M. M., Tang, H., Bowles, M., & Porter, F., 2021. Structured variational inference for simulating populations of radio galaxies, *MNRAS*, **503**(3), 3351–3370.
- Becker, R. H., White, R. L., & Helfand, D. J., 1995. The FIRST Survey: Faint Images of the Radio Sky at Twenty Centimeters, *The Astrophysical Journal*, **450**, 559.
- Bieringer, S., Butter, A., Diefenbacher, S., Eren, E., Gaede, F., Hundhausen, D., Kasieczka, G., Nachman, B., Plehn, T., & Trabs, M., 2022. Calomplification – the power of generative calorimeter models.
- Bonaldi, A. & et al., 2021. Square Kilometre Array Science Data Challenge 1: analysis and results, *MNRAS*, **500**(3), 3821–3837.
- Bowles, M., Scaife, A. M. M., Porter, F., Tang, H., & Bastien, D. J., 2020. Attention-gating for improved radio galaxy classification, *MNRAS*, **501**(3), 4579–4595.
- Bowles, M., Bromley, M., Allen, M., & Scaife, A., 2021. E(2) equivariant self-attention for radio astronomy.
- Brier, G. W., 1950. Verification of forecasts expressed in terms of probability, *Monthly Weather Review*, **78**(1), 1–3.
- Buhmann, E., Diefenbacher, S., Eren, E., Gaede, F., Kasieczka, G., Korol, A., & Krüger, K., 2021. Getting high: High fidelity simulation of high granularity calorimeters with high speed, *Computing and Software for Big Science*, **5**(1).
- Buhmann, E., Diefenbacher, S., Eren, E., Gaede, F., Hundhausen, D., Kasieczka, G., Korcari, W., Krüger, K., McKeown, P., & Rustige, L., 2022. Hadrons, better, faster, stronger, *Machine Learning: Science and Technology*, **3**(2).
- Butter, A., Diefenbacher, S., Kasieczka, G., Nachman, B., & Plehn, T., 2021. Ganplying event samples, *SciPost Physics*, **10**(6).
- Capetti, A., Massaro, F., & Baldi, R. D., 2017a. Fricat: A first catalog of fr i radio galaxies, *A&A*, **598**, A49.
- Capetti, A., Massaro, F., & Baldi, R. D., 2017b. Friicat: A first catalog of fr ii radio galaxies, *A&A*, **601**, A81.
- Carilli, C., Furlanetto, S., Briggs, F., Jarvis, M., Rawlings, S., & Falcke, H., 2004. Probing the dark ages with the square kilometer array, *New Astronomy Reviews*, **48**(11–12), 1029–1038.
- Cheng, T.-Y., Conselice, C. J., Aragón-Salamanca, A., Li, N., Bluck, A. F. L., Hartley, W. G., Annis, J., Brooks, D., Doel, P., García-Bellido, J., James, D. J., Kuehn, K., Kuropatkin, N., Smith, M., Sobreira, F., & Tarle, G., 2020. Optimizing automatic morphological classification of galaxies with machine learning and deep learning using Dark Energy Survey imaging, *Monthly Notices of the Royal Astronomical Society*, **493**(3), 4209–4228.
- Dosovitskiy, A., Beyer, L., Kolesnikov, A., Weissenborn, D., Zhai, X., Unterthiner, T., Dehghani, M., Minderer, M., Heigold, G., Gelly, S., Uszkoreit, J., & Houlsby, N., 2020. An image is worth 16x16 words: Transformers for image recognition at scale.
- Fanaroff, B. L. & Riley, J. M., 1974. The morphology of extragalactic radio sources of high and low luminosity, *MNRAS*, **167**, 31P–36P.
- Frid-Adar, M., Klang, E., Amitai, M., Goldberger, J., & Greenspan, H., 2018. Synthetic data augmentation using gan for improved liver lesion classification.
- Gendre, M. A. & Wall, J. V., 2008. The combined nvss-first galaxies (config) sample - i. sample definition, classification and evolution, *MNRAS*, **390**(2), 819–828.
- Gendre, M. A., Best, P. N., & Wall, J. V., 2010. The combined nvss-first galaxies (config) sample - ii. comparison of space densities in the fanaroff-riley dichotomy, *MNRAS*, **404**(4), 1719–1732.
- Goodfellow, I. J., Pouget-Abadie, J., Mirza, M., Xu, B., Warde-Farley, D., Ozair, S., Courville, A., & Bengio, Y., 2014. Generative adversarial networks.
- Gowal, S., Rebuffi, S.-A., Wiles, O., Stumberg, F., Calian, D. A., & Mann, T., 2021. Improving robustness using generated data.
- Griese, F., Kummer, J., & Rustige, L., 2022. 10.5281/zenodo.7120632.
- Gulrajani, I., Ahmed, F., Arjovsky, M., Dumoulin, V., & Courville, A., 2017. Improved training of wasserstein gans.
- Jonas, J. & MeerKAT Team, 2016. The MeerKAT Radio Telescope, in *MeerKAT Science: On the Pathway to the SKA*, p. 1.
- Krizhevsky, A., Sutskever, I., & Hinton, G. E., 2012. Imagenet classification with deep convolutional neural networks, in *Proceedings of the 25th International Conference on Neural Information Processing Systems - Volume 1*, NIPS’12, p. 1097–1105, Curran Associates Inc., Red Hook, NY, USA.
- Kummer, J., Rustige, L., Griese, F., Borrás, K., Brüggén, M., Connor, P. L. S., Gaede, F., Kasieczka, G., & Schleper, P., 2022. Radio galaxy classification with wgan-supported augmentation, in *INFORMATIK 2022, Lecture Notes in Informatics (LNI) - Proceedings*, vol. P-326, pp. 469–478, Gesellschaft für Informatik, Bonn.
- Lintott, C. J., Schawinski, K., Slosar, A., Land, K., Bamford, S., Thomas, D., Raddick, M. J., Nichol, R. C., Szalay, A., Andreescu, D., Murray, P., & Vandenberg, J., 2008. Galaxy Zoo: morphologies derived from visual inspection of galaxies from the Sloan Digital Sky Survey, *MNRAS*, **389**(3), 1179–1189.
- Lukic, V., Brüggén, M., Mingo, B., Croston, J. H., Kasieczka, G., & Best, P. N., 2019. Morphological classification of radio galaxies: capsule networks versus convolutional neural networks, *MNRAS*, **487**(2), 1729–1744.
- Ma, Z., Zhu, J., Li, W., & Xu, H., 2018. Radio galaxy morphology generation using residual convolutional autoencoder and gaussian mixture models, in *25th IEEE ICIP*, pp. 3044–3048.
- Ma, Z., Xu, H., Zhu, J., Hu, D., Li, W., Shan, C., Zhu, Z., Gu, L., Li, J., Liu, C., & Wu, X., 2019. A Machine Learning Based Morphological Classification of 14,245 Radio AGNs Selected from the Best-Heckman Sample, *ApJS*, **240**(2), 34.
- Ma, Z., Zhu, J., Zhu, Y., & Xu, H., 2019. Radio galaxy morphology simulation via residual conditional variational autoencoder, in *15th International Conference on Computational Intelligence and Security (CIS)*, pp. 151–155.
- Maslej-Krešňáková, V., El Boucheffry, K., & Butka, P., 2021. Morphological classification of compact and extended radio galaxies using convolutional neural networks and data augmentation techniques, *MNRAS*, **505**(1), 1464–1475.
- McNamara, B. R. & Nulsen, P. E. J., 2007. Heating Hot Atmospheres with Active Galactic Nuclei, *ARA&A*, **45**(1), 117–175.
- Mingo, B., Croston, J. H., Hardcastle, M. J., Best, P. N., Duncan, K. J., Morganti, R., Rottgering, H. J. A., Sabater, J., Shimwell, T. W., Williams, W. L., Brienza, M., Gurkan, G., Mahatma, V. H., Morabito, L. K., Prandoni, I., Bondi, M., Ineson, J., & Mooney, S., 2019. Revisiting the Fanaroff-Riley dichotomy and radio-galaxy morphology with the LOFAR Two-Metre Sky Survey (LoTSS), *MNRAS*, **488**(2), 2701–2721.
- Miraghaei, H. & Best, P. N., 2017. The nuclear properties and extended morphologies of powerful radio galaxies: the roles of host galaxy and environment, *MNRAS*, **466**(4), 4346–4363.
- Mostert, R. I. J., Duncan, K. J., Röttgering, H. J. A., Polsterer, K. L., Best, P. N., Brienza, M., Brüggén, M., Hardcastle, M. J., Jurlin, N., Mingo, B., Morganti, R., Shimwell, T., Smith, D., & Williams, W. L., 2021. Unveiling the rarest morphologies of the LOFAR Two-metre Sky Survey radio source population with self-organised maps, *A&A*, **645**, A89.
- Nair, P. B. & Abraham, R. G., 2010. A Catalog of Detailed Visual Mor-



- phological Classifications for 14,034 Galaxies in the Sloan Digital Sky Survey, *ApJS*, **186**(2), 427–456.
- Petrillo, C. E., Tortora, C., Chatterjee, S., Vernardos, G., Koopmans, L. V. E., Verdoes Kleijn, G., Napolitano, N. R., Covone, G., Schneider, P., Grado, A., & McFarland, J., 2017. Finding strong gravitational lenses in the Kilo Degree Survey with Convolutional Neural Networks, *MNRAS*, **472**(1), 1129–1150.
- Porter, F., 2020. 10.5281/zenodo.4288837.
- Proctor, D. D., 2011. Morphological annotations for groups in the first database, *The Astrophysical Journal Supplement Series*, **194**(2), 31.
- Radford, A., Metz, L., & Chintala, S., 2015. Unsupervised Representation Learning with Deep Convolutional Generative Adversarial Networks, *arXiv e-prints*, p. arXiv:1511.06434.
- Sadeghi, M., Javaherian, M., & Miraghaei, H., 2021. Morphological-based classifications of radio galaxies using supervised machine-learning methods associated with image moments, *The Astronomical Journal*, **161**(2), 94, Publisher: American Astronomical Society.
- Salimans, T., Goodfellow, I., Zaremba, W., Cheung, V., Radford, A., & Chen, X., 2016. Improved techniques for training gans.
- Samudre, A., George, L. T., Bansal, M., & Wadadekar, Y., 2021. Data-efficient classification of radio galaxies, *MNRAS*, **509**(2), 2269–2280.
- Scaife, A. M. M. & Porter, F., 2021. Fanaroff-Riley classification of radio galaxies using group-equivariant convolutional neural networks, *MNRAS*, **503**(2), 2369–2379.
- Schmidt, K., Geyer, F., Fröse, S., Blumenkamp, P. S., Brüggén, M., de Gasperin, F., Elsässer, D., & Rhode, W., 2022. Deep learning-based imaging in radio interferometry, *A&A*, **664**, A134.
- Slijepcevic, I. V., Scaife, A. M. M., Walmsley, M., & Bowles, M., 2022. Learning useful representations for radio astronomy "in the wild" with contrastive learning.
- Slijepcevic, I. V., Scaife, A. M. M., Walmsley, M., Bowles, M., Wong, O. I., Shabala, S. S., & Tang, H., 2022. Radio Galaxy Zoo: using semi-supervised learning to leverage large unlabelled data sets for radio galaxy classification under data set shift, *MNRAS*, **514**(2), 2599–2613.
- Tang, H., Scaife, A. M. M., & Leahy, J. P., 2019. Transfer learning for radio galaxy classification, *MNRAS*, **488**(3), 3358–3375.
- van Haarlem, M. & et al., 2013. LOFAR: The LOw-Frequency ARray, *A&A*, **556**, A2.
- Vavilova, I. B., Dobrycheva, D. V., Vasylenko, M. Y., Elyiv, A. A., Melnyk, O. V., & Khramtsov, V., 2021. Machine learning technique for morphological classification of galaxies from the SDSS. I. Photometry-based approach, *A&A*, **648**, A122.
- Vazza, F., Wittor, D., Di Federico, L., Brüggén, M., Brienza, M., Brunetti, G., Brighenti, F., & Pasini, T., 2022. Life cycle of cosmic-ray electrons in the intracluster medium, *arXiv e-prints*, p. arXiv:2210.01591.
- Wu, C., Wong, O. I., Rudnick, L., Shabala, S. S., Alger, M. J., Banfield, J. K., Ong, C. S., White, S. V., Garon, A. F., Norris, R. P., Andernach, H., Tate, J., Lukic, V., Tang, H., Schawinski, K., & Diakogiannis, F. I., 2019. Radio Galaxy Zoo: CLARAN - a deep learning classifier for radio morphologies, *MNRAS*, **482**(1), 1211–1230.
- Zhu, X., Liu, Y., Qin, Z., & Li, J., 2017. Data augmentation in emotion classification using generative adversarial networks.

## APPENDIX A: GENERATED AND REAL IMAGES

Here we show a random sample of 24 real images in Fig. A1 and 24 generated images in Fig. A2 in order to give a visual impression of the diversity of the data.

## APPENDIX B: CLASSIFIER ARCHITECTURES

Detailed information about the architecture of the implemented classifiers is given in this appendix. The structure and the corresponding number of parameters for the FCN is given in Table B1 and the CNN in Table B2.

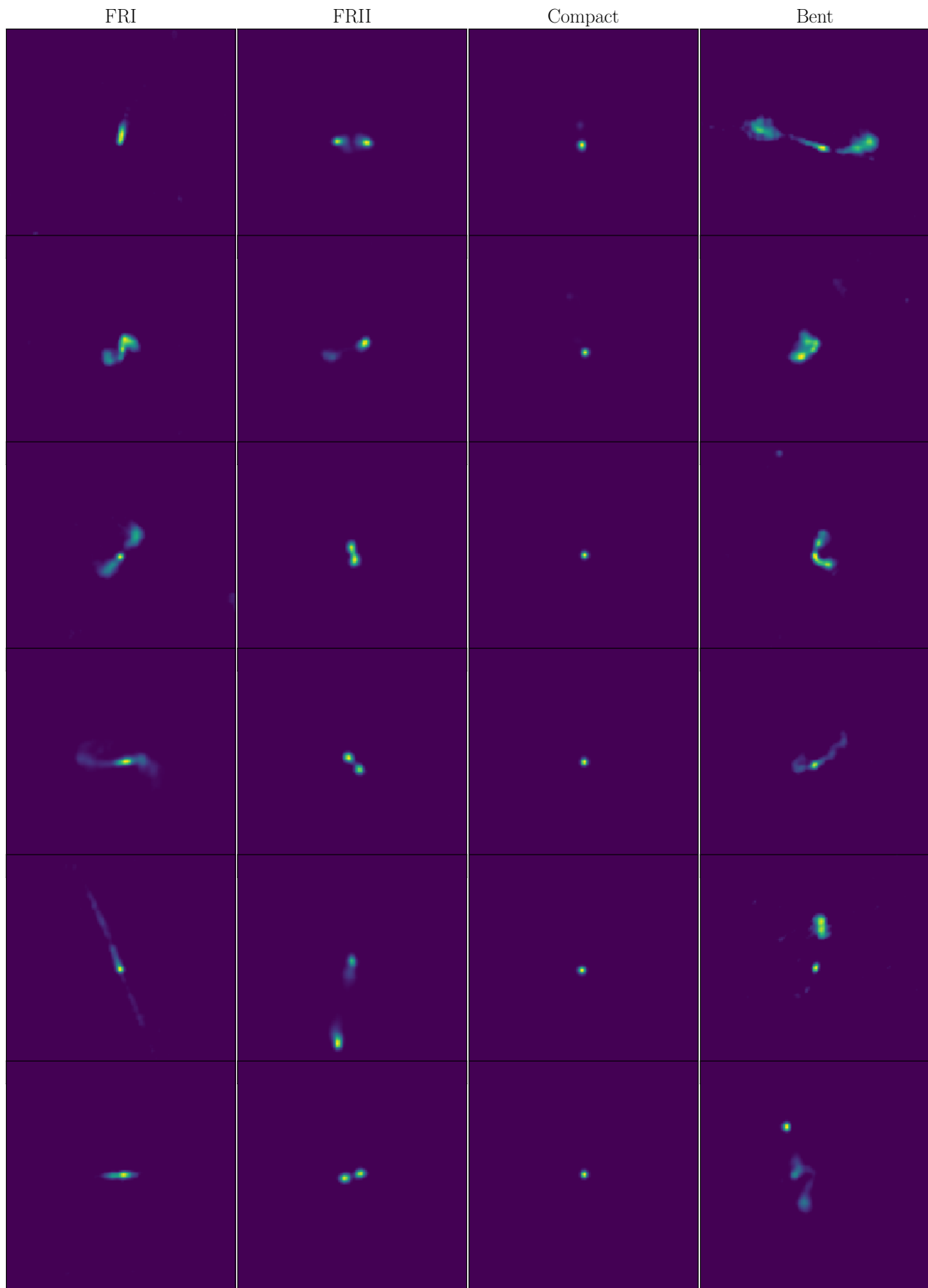


**Figure A1.** Real examples for each class.

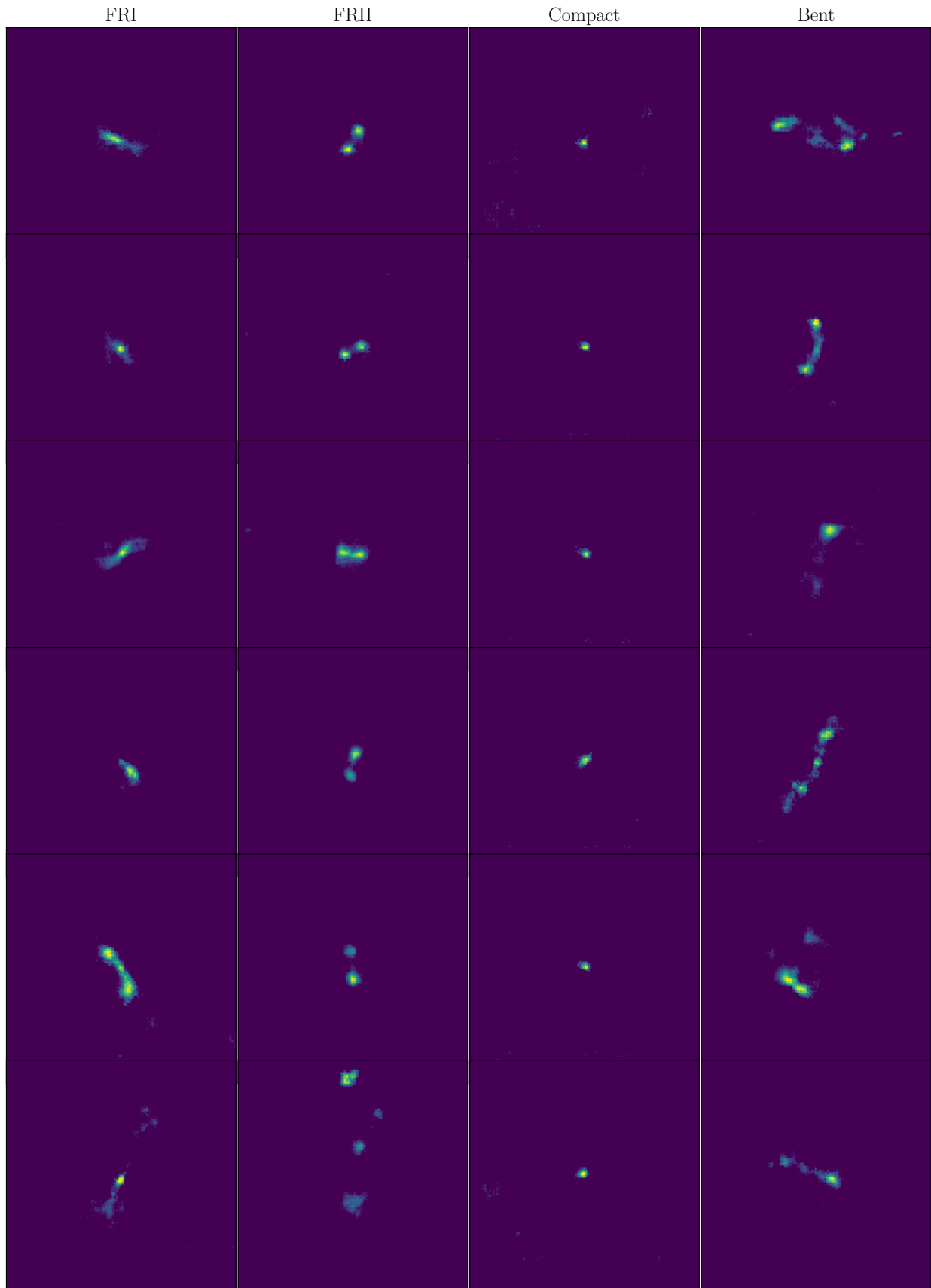


**Figure A2.** Generated examples for each class.

**Table B1.** Parameters of the Fully Connected Neural Network classifier.

Layer	Name	Input channels	Depth	Activation	Parameters
1	Fully Connected 1	128 x 128	250	Leaky ReLU	4,096,250
2	Fully Connected 2	250	250	Leaky ReLU	62,750
3	Fully Connected 3	250	250	Leaky ReLU	62,750
4	Fully Connected 4	250	250	Leaky ReLU	62,750
5	Fully Connected 5	250	4		1,004
6	Softmax				
Total parameters:					4,285,504

**Table B2.** Parameters of the Convolutional Neural Network classifier.

Layer	Name	Kernel size	stride	Input channels	Depth	Activation	Regularizer	Parameters
1	Conv1	3 x 3	2	1	8	Leaky ReLU	Layer Norm	8264
2	Conv2	3 x 3	2	8	16	Leaky ReLU	Layer Norm	3200
3	Conv3	3 x 3	2	16	32	Leaky ReLU	Layer Norm	5120
4	Conv4	3 x 3	2	32	32	Leaky ReLU	Layer Norm	9344
5	Conv5	2 x 2	1	32	16	Leaky ReLU	-	2048
6	Fully Connected 1			7 x 7 x 16	100	Leaky ReLU	-	78500
7	Fully Connected 2			100	4	ReLU	-	404
8	Softmax							
Total parameters:								104,832

This paper has been typeset from a  $\text{\LaTeX}$  file prepared by the author.